Optical Clearing for Improved Contrast in Second Harmonic Generation Imaging of Skeletal Muscle

Sergey Plotnikov,*†‡ Vaibhav Juneja,* Ariel B. Isaacson,* William A. Mohler,*‡ and Paul J. Campagnola†‡
*Department of Genetics and Developmental Biology, †Department of Cell Biology, and ‡Center for Cell Analysis and Modeling, University of Connecticut Health Center, Farmington, Connecticut 06030

ABSTRACT Using second harmonic generation (SHG) imaging microscopy, we have examined the effect of optical clearing with glycerol to achieve greater penetration into specimens of skeletal muscle tissue. We find that treatment with 50% glycerol results in a 2.5-fold increase in achievable SHG imaging depth. Signal processing analyses using fast Fourier transform and continuous wavelet transforms show quantitatively that the periodicity of the sarcomere structure is unaltered by the clearing process and that image quality deep in the tissue is improved with clearing. Comparison of the SHG angular polarization dependence also shows no change in the supramolecular organization of acto-myosin complexes. By contrast, identical treatment of mouse tendon (collagen based) resulted in a strong decrease in SHG response. We suggest that the primary mechanism of optical clearing in muscle with glycerol treatment results from the reduction of cytoplasmic protein concentration and concomitant decrease in the secondary inner filter effect on the SHG signal. The lack of glycerol concentration dependence on the imaging depth indicates that refractive index matching plays only a minor role in the optical clearing of muscle. SHG and optical clearing may provide an ideal mechanism to study physiology in highly scattering skeletal or cardiac muscle tissue with significantly improved depth of penetration and achievable imaging depth.

INTRODUCTION

In recent years several nonlinear optical (NLO) techniques, including second harmonic generation (SHG) (1–7), third harmonic generation (THG) (8,9), and coherent anti-stokes Raman scattering (CARS) (10–12), have emerged as powerful new high resolution imaging modalities for biological applications. Much like multiphoton-excited fluorescence microscopy, each of these methods provides intrinsic optical sectioning due to the required high peak power required for efficient NLO ''excitation''. Furthermore, the near infrared wavelengths that are typically used allow penetration of several hundred microns into highly turbid tissues. Each of these modalities can often provide more detailed information than possible by fluorescence or classical microscopy techniques. For example, CARS probes vibrational motions of proteins and nucleic acids and thus affords the ability for specific chemical imaging combined with high spatial resolution (11). SHG arises from the highly organized assembly of molecules in noncentrosymmetric environments and has been used to image cellular membranes with great specificity (13) and provide data regarding the organization and symmetries of structural protein arrays in tissues (1). THG is highly sensitive to changes in refractive index and can be used to resolve interfacial regions of cells and tissues (8). A common and powerful feature of all the methods is that they can rely entirely on endogenous species to provide the contrast.

The ability to section through thick tissues and provide molecular and supramolecular level information on the spatial organization of proteins positions SHG as an imaging modality with vast potential for both research and clinical applications. Indeed, an array of tissues including tendon (15), cornea (16), muscle (1,17), and bone (18) as well as microtubule assemblies in live cells (1,19) and developing tissues (9) have recently been imaged and studied by SHG imaging microscopy. Some of this work has focused on understanding the physical and chemical underpinnings of the contrast mechanism in tissues. For example, we studied the SHG contrast from several regions in *Caenorhabditis elegans* nematodes, including muscle assemblies (body wall sarcomeres, pharynx) as well as microtubule assemblies (centrosomes, mitotic spindles), by comparison of the images with those resulting from specific GFP labeling (1). The symmetries of these assemblies were investigated through SHG polarization anisotropy analysis and were found to be consistent with arising from the electric dipole interaction. Furthermore, these data provided more direct structural information than possible by using only GFP labels. This is because the SHG directly visualizes the structural anisotropy, rather than relying on indirect inference from a fluorescent dye label where this information is often lost. Other recent work has examined the plausibility of the method in more clinically related applications. For example, Jain and co-workers used SHG to image the collagen content in tumors in mouse and perform semiquantitative measurements of the collagen concentration (20). Additionally, Tromberg and co-workers

Submitted May 19, 2005, and accepted for publication September 21, 2005.

Address reprint requests to Paul J. Campagnola, University of Connecticut Health Center, Dept. of Cell Biology, Center for Cell Analysis and Modeling, MC-1507 263 Farmington Ave., Farmington, CT 06030. Tel.: 860-679-4354; Fax: 860-679-1039; E-mail: campagno@neuron.uchc.edu. Or to William A. Mohler, University of Connecticut Health Center, Dept. of Genetics and Developmental Biology, Center for Cell Analysis and Modeling, 263 Farmington Ave., Farmington, CT 06030. Tel.: 860-679-1833; Fax: 860-760-6140; E-Mail: wmohler@neuron.uchc.edu.

0006-3495/06/01/328/12 $2.00

doi: 10.1529/biophysj.105.066944

showed that this modality could be used to image dynamical aspects of blood flow by monitoring the collagen in the vessels (21).

A potentially limiting aspect of SHG imaging lies in the directionality of the emission. Due to its coherent nature, the SHG wave is primarily emitted in the forward direction. Indeed, in the limit of a nonscattering sample with uniformly aligned molecules (or more precisely, dipole moments), essentially all the SHG is forward directed (4). For thicker, turbid, highly scattering specimens, a fraction of the SHG is backscattered. This mode of SHG imaging is convenient to implement as it requires minimal modification of an existing multiphoton fluorescence microscope. Furthermore, this configuration allows imaging of the top layers of intact skin or whole animals that cannot be performed in a transmitted geometry. This method has been used primarily to image collagen, which produces SHG much more efficiently than other protein arrays (e.g., acto-myosin, tubulin) (1). On the other hand, the bulk of the SHG is still forward directed and only a fraction of the light is backscattered. Furthermore, the resulting coherence and polarization anisotropy of the backward-directed component to date has not been thoroughly investigated. It is likely that much of the structural information encoded in the SHG signal in the forward direction will be lost in the backward signal due to the multiple scattering events.

Our work to date has utilized SHG exclusively in the forward direction, and we have characterized some aspects of the polarization anisotropy of the signal (1). It would be advantageous to exploit the purely coherent forward-directed signal, which retains the anisotropy, and simultaneously achieve significant penetration into highly scattering tissues, including muscle. Our approach in this work is to combine SHG with the optical clearing effect to achieve this goal. In this process, a reagent of high refractive index (e.g., glycerol or sugar alcohols) is added to the tissue to increase its transparency. There is increasing interest in this idea with the advent of advances in deep tissue imaging, where recent studies have examined the clearing potential of hyperosmotic agents (glycerol, PEG, and DMSO) in such diverse tissues as skin (22–24), blood (25), dura mater (26), and gastric tissue (27). The increase in penetration in these studies was measured using transmitted light and/or optical coherence tomography (OCT). It was demonstrated in these examples that the depth of light penetration increased to ~100–300%. However, in these experiments the physiological and structural similarities between treated and untreated samples were not explicitly examined.

Although OCT can be used to obtain cross sectional images relatively deep into tissue, the axial resolution is limited by the bandwidth of the excitation source and the best attainable values are 10–20 microns. Superior axial resolution is obtainable by SHG (~1 micron) and it is, in principle, an imaging modality that would greatly benefit from the use of optical clearing to provide increased imaging depth with excellent resolution in all three dimensions. However, Tromberg and co-workers (28) showed that for the case of collagen (rat tail tendon and RAFT) the optical clearing process using glycerol not only did not improve the transparency in the SHG images but also resulted in a significant decrease in the SHG intensity for both specimens. Conversely, improved transparency was observed in the transmitted light images. Since the SHG should be a more sensitive probe of the underlying structure in the array, these results suggest that the collagen assembly was adversely affected.

Our interests here lie in examining whether optical clearing by glycerol is an effective means to improve image depth and quality in three-dimensional (3-D) SHG imaging of muscle tissue. Since 1949, when Szent-Gyorgyi (29) introduced the use of glycerol to extract muscle, this method has become a typical approach for studying muscle biology. The method is used both to isolate fibers for storage as well as to perform physiological measurements. Numerous experiments showed that immersing muscle in glycerol does not significantly change the chemical and structural properties of the muscle contractile system (30–32). Specifically, antibody labeling showed that myosin remained localized in the muscle sarcomere after treatment. Moreover, Huxley's seminal electron microscopy work showed the similarity of the overall sarcomere structure between native and 50% glycerol extracted fibers (31). Additionally, several studies showed the contractile properties (33,34) of extracted muscle remained intact. However, since this treatment permeabilizes cellular membranes, and thus extracts a fraction of the cytoplasmic proteins, this method can significantly decrease light absorption and scattering within a tissue and provide much greater penetration into highly scattering tissue.

Here we present data on optical clearing of explanted mouse muscle, using 3-D SHG imaging on intact tissue, and show that transparency is substantially increased (~2.5-fold) with a concurrent improvement in image quality deep in the tissue. We have performed several quantitative analyses to show that the muscle fiber structure is not significantly altered. The resulting sarcomere periodicity is examined using both Fourier analysis as well as wavelet transforms, and no changes are found in the sarcomere length upon clearing. The polarization dependence of the SHG signals is a highly sensitive probe to molecular organization of the proteins in the array. We find that this angular dependence is unchanged between the cleared and uncleared muscle specimens, indicating the symmetry and organization of the acto-myosin complexes is not significantly altered in the clearing process. Furthermore, the integrated SHG intensity remains nearly constant after clearing, consistent with the retention of properly assembled myosin. We suggest that optical clearing may become a general method to provide increased transparency in some tissues when used in conjunction with coherent nonlinear imaging modalities of SHG, THG, and CARS.

EXPERIMENTAL METHODS

Sample preparation

The muscle and tendon samples were dissected from adult CD1 mice. The mouse was anaesthetized by CO_2 narcosis and sacrificed, and the lower limbs and tail were dissected. Snips of quadriceps femoris or gastrocnemius muscles were dissected by a 4.0 mm outer diameter × 80 mm skeletal muscle biopsy needle (Popper & Sons, Inc., New Hyde Park, NY), briefly washed in phosphate buffered saline (PBS) (0.137 mM NaCl, 2.7 mM KCl, 8.0 mM Na_2HPO_4, 1.9 mM NaH_2PO_4), immersed into clearing media, and imaged immediately. As clearing media, we used either absolute glycerol (Fisher Scientific, Hampton, NH) or solution containing 50% glycerol, 70 mM NaCl, 1 mM KCl, 1.5 mM $MgCl_2$, 10 mM imidazole-HCl pH 7.0, 5 mM EGTA, 1 mM PMSF. To isolate tail tendon, the skin was pulled from the tail and strips of tendon collagen were carefully detached from the bones, briefly washed in PBS, and kept in the same clearing solution at +4°C. Before imaging, the tendon was cut into smaller fragments (1 cm long), mounted on the microscope slide, and immersed in the clearing solution and secured under a silicone grease-mounted coverslip. 3-D stacks of all samples were acquired at time points between 10 min and 24 h after glycerol treatment.

We initially attempted to perform the measurements in a perfusion chamber; however, because of the high viscosity of glycerol, its perfusion into the chamber caused movement of the tissue sample. Similarly, the imaging control data (see below in Results) in the absence of glycerol could not be performed on the same specimen as the treated muscle. Instead, for the time course studies, the snip of muscle was mounted into the glycerol solution on a regular slide, where the time between immersing the tissue into glycerol-containing solution and beginning data acquisition was ~5–10 min. Analysis of the difference between the 10 and the 30 min time points suggests little clearing was missed in the short interval before the start of imaging.

SHG imaging system

Detailed descriptions of the SHG microscope have been given previously (1,18), and only a brief outline will be provided here. The SHG imaging experiments were performed on a modified Olympus Fluoview 300 confocal scan head mounted on a fixed stage Olympus BX61 upright microscope (Olympus USA, Melville, NY). The laser system is a 10 watt Verdi pumped femtosecond titanium sapphire oscillator (MIRA 900-F; Coherent, Santa Clara, CA), characterized by a pulse width of ~100 fs at a 76 MHz repetition rate, and is operated at 900 nm. The average power at the sample was ~50 mW or ~650 pJ pulse energy, with a 0.8 numerical aperture (NA) water immersion long working distance objective lens. The 1 mrad divergence of the Ti:sapphire laser was compensated before the scan head with a 1 m focal length lens. For all imaging not involving polarization analysis, the laser fundamental was circularly polarized for the excitation. The SHG was collected in the forward direction, where a long working distance 40 × 0.8 NA water immersion objective and a 0.9 NA condenser are used for excitation and signal collection, respectively. The SHG signal is first reflected with a 450 nm hard reflector (bandwidth ±25 nm; CVI Laser, Albuquerque, NM), then isolated from the laser fundamental and any fluorescence by 1 mm color glass (BG-39) and a 450 nm band-pass filter (10 nm full width at half-maximum, and detected by a photon-counting photomultiplier module (Hamamatsu 7421; Bridgewater, NJ). The TTL pulses from this module are integrated by the Olympus acquisition electronics. The SHG wavelength was verified by the use of a fiber optic based spectrometer (Ocean Optics USB2000, Dunedin, FL).

The polarization dependence of the SHG signal was determined by rotating the plane of polarization of the excitation with respect to the fiber axis of muscle tissue and then measuring the entire SHG signal (no output polarization analysis) as a function of this angle. Although this dependence can be determined by rotating the input laser polarization with a half-wave plate, this method can be inaccurate due to ellipticity introduced by steering optics and the galvo scanners. Thus, we fix the laser polarization (using a quarter-wave plate to compensate for downstream ellipticity) and rotate the tissue with a centering circular rotation stage. The data are taken at high zoom from a region in the middle of the field to ensure true centering of the sample, i.e., there exists rotational invariance with respect to translation.

Image analysis

3-D image projections were created from the Olympus Fluoview TIFF format using ImageJ (http://rsb.info.nih.gov/ij). *x-z* projections were also made with ImageJ by digital reslicing of an 8μm-thick *x-z* section through the image volume. ImageJ was also used to obtain fast Fourier transforms (FFTs) of the sarcomeric structures to quantitatively compare the local spatial frequencies of the uncleared and cleared tissues.

We also use continuous wavelet transforms (CWT) as a metric of the image quality as a function of depth in the tissue, where this analysis was performed with MATLAB (The MathWorks, Natick, MA). In the CWT analysis, the width of the wavelet is varied and the correlation with the frequency components of the image is calculated for a series of differing window widths or scale (35). The CWT transform generally expressed for a function x(t) is given by

$$\mathrm{CWT}_x^{\psi}(\tau, s) = s^{-1/2}\int x(t)\psi * \left(\frac{t-\tau}{s}\right)dt, \qquad (1)$$

where s is scale and ψ^* is the complex conjugate of the wavelet function. The correlation coefficients, C, as a function of scale and position are then calculated by

$$C(scale, position) = \int_{-\infty}^{\infty} f(t)\psi(scale, position, t)dt, \quad (2)$$

where $f(t)$ is the signal to be analyzed and ψ is the mother wavelet. We use the Morlet wavelet, which is the superposition of a sine and Gaussian function and is appropriate for analyzing periodic or quasiperiodic signals. For each optical section where the pixel/micron ratio is 3, the image is broken up into 50 × 50 pixel matrices and the CWT is calculated for each line in the image over a range of scales between 4 and 5. This is repeated for each matrix and for all sections in a 3-D stack. For comparison of the SHG images of control and cleared tissues via a single metric of the image quality, we use the Shannon entropy, which is calculated by

$$WTE_s = -\sum p \ln p, \qquad (3)$$

where p represents the probability of a given coefficient, w, at scale, s, and is defined by

$$p = \frac{p_s}{\sum_i p_{s,i}}. \qquad (4)$$

In this formalism an image with zero entropy would be completely lacking in order, as the sum of the coefficients would approach zero, and would in muscle tissue correspond to the case of completely scrambled or absent sarcomeres. By contrast, more highly ordered or regular signals would have increasingly negative entropy values.

RESULTS

Optical clearing of muscle tissue

As described earlier, other recent reports have used OCT and transmitted light imaging to investigate the effect of optical clearing with glycerol in several tissues. Here we use forward-directed SHG to measure the increase in penetration depth in muscle tissue and achievable imaging depth due to optical clearing by addition of glycerol. We first examine

the effect with 50% glycerol, as the biochemistry of this treatment has been well characterized (31). Fig. 1 shows raw data (*A*) and contrast-stretched (*B*) *x-z* projections as a 24 h time course after this treatment. The muscle fibers are easily distinguished in this representation, and the improvement in transparency is readily observed with increasing time after treatment. We quantified these findings by plotting the average SHG intensity of each optical section as a function of depth during the observation period, and these are shown in Fig. 1 *C*. Although the diffusion of the glycerol into the muscle is slow, some increase in penetration is seen within 30 min, and significant clearing occurs within 120 min. At depths up to ~60 microns, little increase in intensity is seen between 2 and 24 h of exposure to glycerol. However, deeper in the tissue some additional clearing occurs. By contrast, the control experiment of imaging muscle tissue in Tissue-Tek OCT compound (Sakura Finetek, Torrance, CA) over 24 h showed no optical clearing (data not shown).

All the time points display an exponential falloff in SHG intensity with depth. The intensity, $I(z)$, as a function of depth, z, is expected to scale as

$$I(z) = I(0)e^{-\mu_{\text{eff}}z}, \tag{5}$$

where $I(0)$ is the intensity at the top of the stack and μ_{eff} is the effective attenuation coefficient and is the reciprocal of the mean penetration depth (36). This quantity is related to the reduced scattering and absorption coefficients, μ_a and μ_s', respectively, by

$$\mu_{\text{eff}} = [3\mu_a(\mu_a + \mu_s')]^{1/2}. \tag{6}$$

For SHG imaging, the total absorption and scattering coefficients are the sum of the terms corresponding to the fundamental (900 nm) and SHG wavelengths (450 nm). Due to the more complex scenario over one-color scattering measurements, we thus use ''achievable imaging depth'' in lieu of the mean penetration depth. The contribution from absorption at the 900 nm wavelength is not significant, whereas, as will be shown below, absorption of the SHG wave has a large effect on the image contrast. For the case of multiple scattering in highly turbid tissue, such as muscle, the ordinary scattering coefficient is more properly expressed as the reduced scattering coefficient, μ_s':

$$\mu_s' = \mu_s(1 - g), \tag{7}$$

where g is the average cosine of the scattering angle and ranges 0.7–0.95 in most tissues. This factor accounts for the highly forward-directed scattering in tissue and is a measure of the distance needed for the optical energy to become isotropically distributed (36). Fits to Eq. 3 for several trials ($n =$ 12 and 14 for control and optically cleared, respectively) are shown in Fig. 2. Glycerol treatment improved the mean SHG imaging depths (1/*e* point) from 85 to 210 microns, nearly a 2.5-fold improvement over the uncleared tissue. The origin of the large deviation of the data from the exponential fit near the top of the axial profile is described in the Discussion.

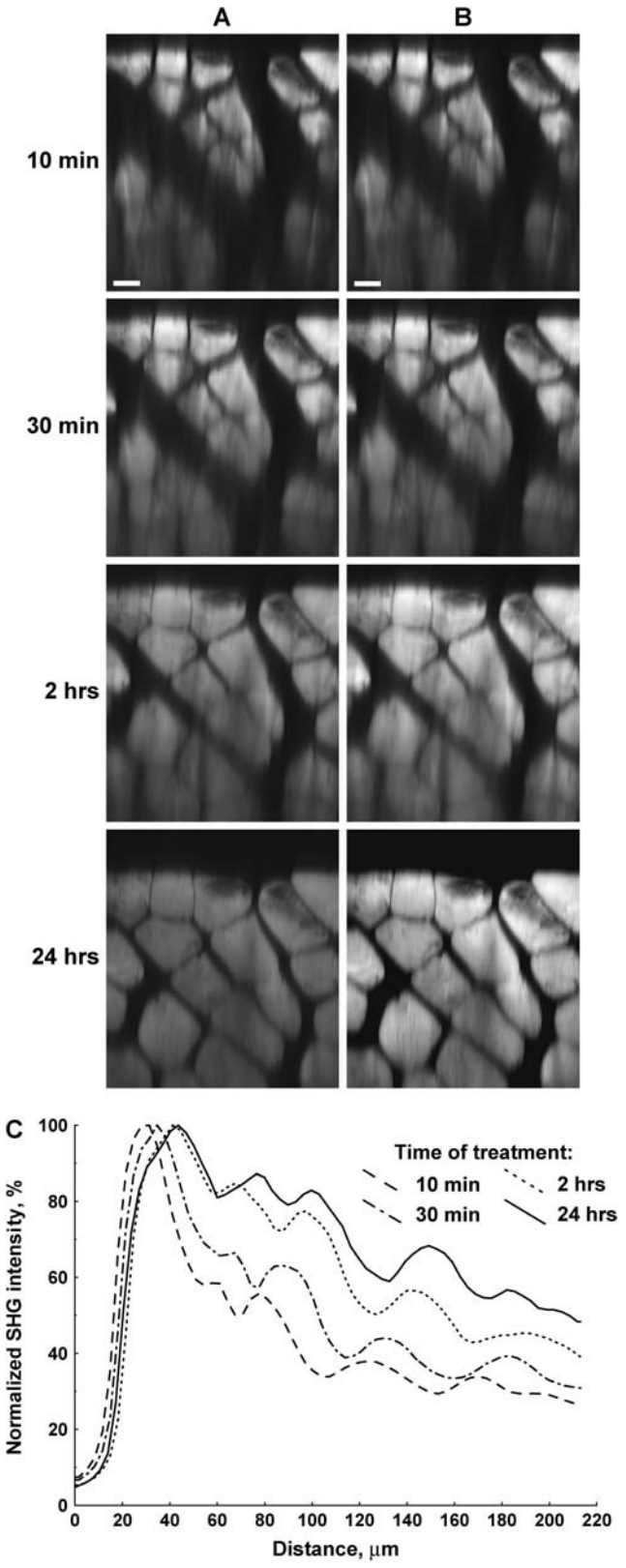

FIGURE 1 SHG imaging probes optical clearing in 50% glycerol-treated explanted mouse muscle. (*A*) SHG *x-z* projections at 10 min, 30 min, 120 min, and 24 h. (*B*) Contrast stretched images of *A*. (*C*) The normalized SHG intensity at various depths after 50% glycerol treatment. Scale bar, 20 microns.

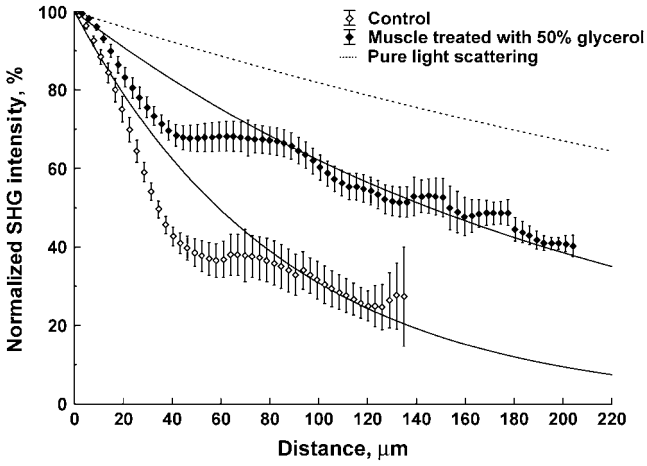

FIGURE 2 Exponential fits to the average of several trials for the depth dependence of the SHG in control and optically cleared tissue with 50% glycerol. These fits result in achievable SHG imaging depths (1/*e*) of 85 and 210 microns, respectively. For comparison, the expected attenuation based solely on scattering with the reported reduced scattering coefficient of 0.5 mm^{-1} is also shown (*dashed line*).

We next verified that the observed depth dependence of the SHG signal did not arise from or was largely influenced by optical aberrations due to a refractive index mismatch with a water immersion lens. Significant spherical aberration of the laser would result in decreased peak intensity and possibly become increasingly significant at greater depths. Although it not rigorous to define a point spread function (PSF) for SHG as it is a coherent process, we can still measure this property for two-photon excited fluorescence at the 900 nm fundamental wavelength to ascertain if there are differences in peak power as a function of depth, and also for specimens with and without 50% glycerol. Since it is not practical to perform these measurements in tissue, they were performed in phantoms containing 100 nm fluorescent beads suspended in 1% agarose (37) in control and 50% glycerol-containing solutions. Using the 0.8 NA water immersion lens, we obtained lateral PSFs (data not shown) for the control of 580–600 nm at depths up to 200 microns. The 50% glycerol-containing phantom was characterized by a range of 560–610 nm, where the relatively small deviations were not correlated with the depth. Thus we conclude that the data in Fig. 2 are reflective of the actual depth-dependent decay of the SHG signal.

One proposed mechanism of optical clearing has been attributed to refractive index matching. (24) To examine if the improvement in SHG imaging depth in muscle arises from this effect, the experiment was repeated with 100% glycerol, where the intracellular refractive index would be higher ($n \sim 1.45$). Fig. 3 displays the *x-z* projections (*A*) and the average SHG intensity of each optical section as a function of depth (*B*) during this 24 h time course. The swelling of the muscle cells is much more pronounced at the 24 h point than was observed with the 50% glycerol treatment. Furthermore, the clearing effect was largely lost by 24 h. These irregularities in the images thus make it difficult to measure the increase in transparency. However, we remained interested in determining the optimal concentration. These experiments were thus repeated for 25% and 75% glycerol, and the depth-dependent decays (1/*e*) were fit to values of 202 and 178 microns, respectively, similar to the 50% treatment (210 microns). Given these comparable results, combined with the extensive biochemical characterization,

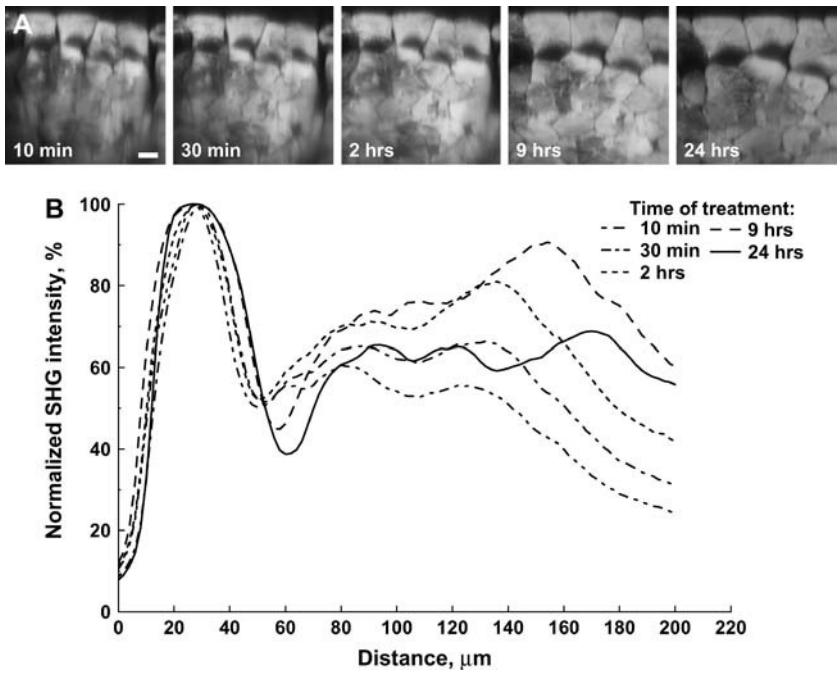

FIGURE 3 Optical clearing of muscle treated with 100% glycerol. (*A*) *x-z* projections of the SHG intensity arising at 10 min, 30 min, 120 min, and 24 h. The muscle fibers are highly swelled at 24 h. (*B*) The average intensity of each optical section as a function of depth at these time points. Scale bar, 20 microns.

we consider the 50% glycerol treatment to be the optimal approach for achieving clearing in muscle. Still, because of the changes in tissue seen with any of the treatments, we next quantitatively examined the muscle structure in the control and cleared tissues.

Quantitative investigation of muscle structure after optical clearing

SHG intensity

Inspection of the fibers near the top of the stack shown in Fig. 1 *A* shows a small loss of intensity (average per pixel) of the SHG signal after glycerol application. This could arise from the fact that the fibers swelled somewhat during the treatment and the number of myofibrils per unit area is reduced. The loss of intensity could also, in principle, be due to loss of properly assembled acto-myosin complexes. Since the SHG intensity is in part determined by the organization of the protein molecules in the array, this modality would be highly sensitive to such adverse effects. Specifically, a randomized distribution of acto-myosin complexes even at high concentration would result in no signal. To investigate these possibilities of a loss of protein content or organization, we compared the overall integrated intensity of the cross sectional area of the fibers in both the control and cleared tissues. We observed that the integrated intensity remains constant (within 15% fluctuation between time points, where $n = 9$). These data indicate that the organized acto-myosin remained localized in the fibers, and that the total content remained constant, but in a larger volume.

This result also sheds light on a question regarding whether the observed SHG intensity depends on the organization at the molecular (and consequently the myofibril level) or that of the fiber cell. The observation that the SHG intensity is conserved with the increase in volume due to swelling implies a linear process. This finding suggests that the swelling of the fiber cell increases the spacing among the myofibrils. We have observed strong SHG from isolated myofibrils (38) and have identified these as the key SHG producing structural units. Thus, if the molecular or myofibril organization was altered in the swelling, a quadratic dependence of the SHG intensity would have been expected. Therefore we conclude that the clearing process does not induce a change at the level of the harmonophore structure. This retention of the spatial organization of the acto-myosin complexes at the molecular level after clearing is further addressed below (in the section Polarization anisotropy measurement of molecular organization) by measuring the polarization dependence of the SHG contrast.

Fast Fourier transform analysis of sarcomere periodicity

Sarcomeres have well-defined characteristic lengths for contracted and extended muscle, and it is important in terms of any functional imaging that these lengths do not change during the clearing process. Fig. 4 *A* shows the SHG image from one optical section of mouse sarcomeres at high zoom and the highly regular periodicity of normal sarcomeres. Note that this data set is from only a thin portion at the top of the whole tissue and not sufficiently thick for the clearing to be readily visualized. The regularity of the signal readily lends itself to analysis via a FFT. To determine the spatial frequencies, FFTs of 15×15 μm subregions from the resulting SHG images were performed using ImageJ software. Histograms of the peak power spectra of the sarcomere lengths during 50% glycerol treatment are shown in Fig. 4 *A*. The two most probable components of the distribution of sarcomere lengths lie in the intervals of $1.5 < x < 1.8$ and $1.8 < x < 2.1$ microns. The less probable intervals at shorter and longer lengths correspond to noise. Although these intervals both show a small increase during the time course, the relative intensities remained nearly constant. To help visualize this finding, the inset in Fig. 4 *B* shows the inverse FFT of the two most probable intervals ($1.5 < x < 1.8$ and $1.8 < x < 2.1$ microns) where the remaining intervals were set to zero and thus eliminate any noise to isolate the SHG frequency components. The green and red data correspond to the FFT-filtered image for the 10 min and 24 h points, respectively. The spatial overlap in the image is high, indicating the sarcomere lengths are largely preserved while obtaining significant optical penetration.

Continuous wavelet transform analysis of image quality

We made use of CWT analysis to further look for any possible adverse morphological effects of the sarcomeres due to the optical clearing process. We use the wavelet transform entropy (WTE_s; Eqs. 3 and 4) as a metric to quantitatively compare the ordered pattern of the sarcomeres in the control and cleared mouse muscle. The resulting entropy values as a function of axial position for 50% treated glycerol tissue are shown in Fig. 5 for the 10 min and 2 h time points. A depth-dependent decrease is seen in both cases as the WTE_s values are dependent upon the absolute signal strengths, which decrease due to the attenuation (scattering and absorption) as described by Eq. 4. We used the absolute entropies to compare the respective image quality as a function of depth for the control and cleared tissue. At the top of the stack, the cleared tissue has lower entropy due to the loss of intensity per unit area from swelling described above. However, from 30 microns through the remaining depth, the WTE_s values are stronger for the cleared sample. The inset shows two corresponding 50×50 pixel image segments at similar depths which demonstrate the relationship between image quality and WTE_s values. This analysis was also performed for the 24 h point, and similar behavior was observed (data not shown), where larger WTE_s values are seen from ~45 microns through the remaining depth. These data indicate that 50% glycerol treatment results in an increase in both the

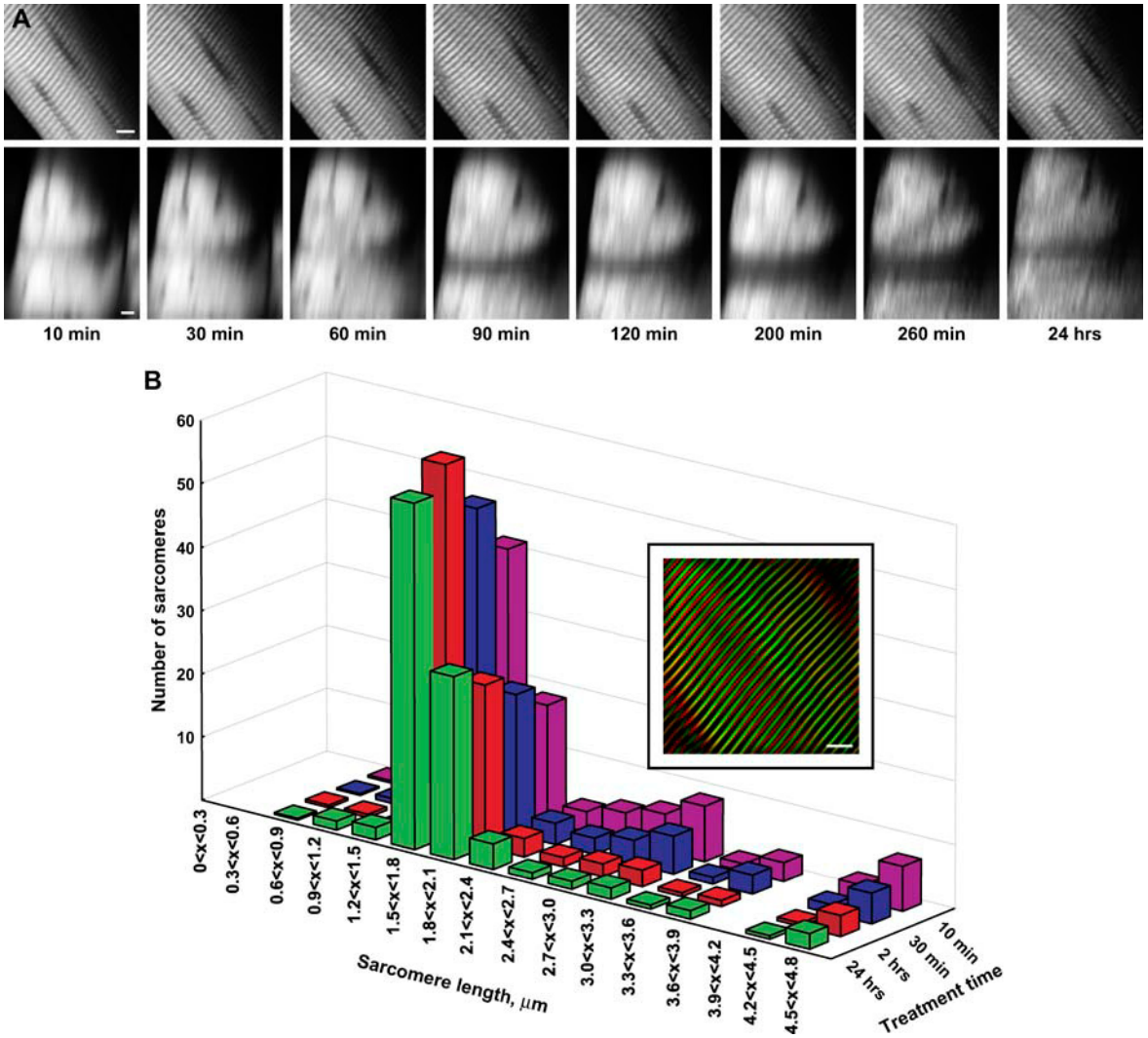

FIGURE 4 FFT analysis of sarcomere periodicity after treatment with 50% glycerol. (*A*) The top and bottom panels show one SHG optical section and the corresponding *x-z* projections during the time course. Scale bar, 5 microns. (*B*) The power spectra from an FFT analysis of the SHG measurements of the sarcomere periodicity are plotted as histograms for the control and optically cleared tissues. The relative intensities in the two most probable intervals of $1.5 < x < 1.8$ and $1.8 < x < 2.1$ microns are largely unchanged in these tissues. The less probable intervals at shorter and longer lengths correspond to noise. The inset shows the inverse FFT image calculated for the control and optically cleared tissues based on the two most probable intervals of $1.5 < x < 1.8$ and $1.8 < x < 2.1$ microns. The green and red data correspond to the FFT-filtered image for the 10 min and 24 h points, respectively.

achievable depth and SHG image quality in deep optical sections of tissue.

Polarization anisotropy measurement of molecular organization

The possibility of alterations occurring on the molecular level due to the glycerol treatment was also considered. SHG is in fact well suited to this task, as polarization analysis can be used to extract information on the supramolecular geometry of the acto-myosin complexes. The general description of the second order polarization $P^{(2)}$ is given by

$$P^{(2)} = a\mathbf{z}(\mathbf{z}\cdot E)^2 + b\mathbf{z}(E\cdot E) + cE(\mathbf{z}\cdot E), \qquad (8)$$

where a, b, and c are coefficients, $\mathbf{z}$ is the unit vector, and E is the electric field vector. This expression contains all the information on the orientation of the molecules in the array. Any changes in the orientation of the molecules within the sarcomeres would appear in the angular polarization dependence of the SHG intensity. We thus compared the polarization profiles of the SHG signal before and after optical clearing. Fig. 6 *A* shows a schematic depicting the relevant axes of the laser propagation and electric field axes and the fiber axis. The resulting SHG intensity as a function of the angle between the fibers and laser polarization is shown in Fig. 6 *B*, where the data are plotted for the same time points as in Fig. 1. Although there are small variations during the time course, there is no systematic correspondence between

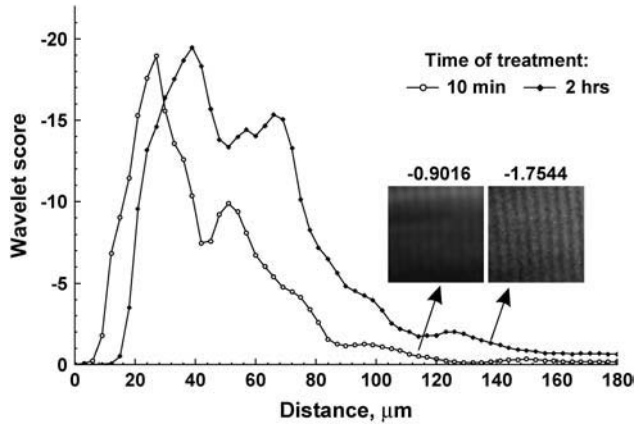

FIGURE 5 WTE_s analysis of image quality after clearing. The absolute WTE_s values are plotted as a function of depth for the control and 2 h time points. The entropy values are higher for the optically cleared sample at depths >30 microns. The inset shows two corresponding 50 × 50 pixel image segments from these time points at similar depths which demonstrate the relationship between image quality and WTE_s values.

the glycerol exposure time and direction of variation. Thus, we concluded that there is no significant change in this structure of the acto-myosin complexes after the clearing process.

Optical clearing of collagen-based tissue

Our results have shown that optical clearing greatly improves SHG imaging of muscle tissue, both in terms of penetration depth and image quality. By contrast, Tromberg and co-workers found greatly reduced backscattered SHG intensity and changes in fiber morphology in glycerol-treated collagen-based specimens (28), suggesting adverse effects on the protein assembly. We investigated the effects of optical clearing on tendon collagen using the forward-directed SHG component to see if such observations depend upon the particular collection geometry. This was a possible scenario, because these two modes of SHG emission probe different features in the supramolecular assemblies. Specifically, the SHG from larger structures (compared to the wavelength of light) is primarily forward directed, whereas the emission from smaller scattering objects is equally directed in the forward and backward directions. For example, Williams et al. (7) recently observed morphologically distinct forward and backward SHG images arising from collagen in tendon.

We show our forward-directed SHG data for mouse tail tendon in Fig. 7 *A*, where the top panel in (*A*) shows the temporal evolution of the SHG signal after treatment with 50% glycerol for a single optical section. The changes throughout the entire stack (*x-z* projections) are shown in the bottom panel of Fig. 7 *A*, where both a loss of intensity and significant swelling of the whole specimen are observed. The integrated intensity for each image is plotted in the bar graph in Fig. 7 *b*, where an~5-fold loss of intensity is observed

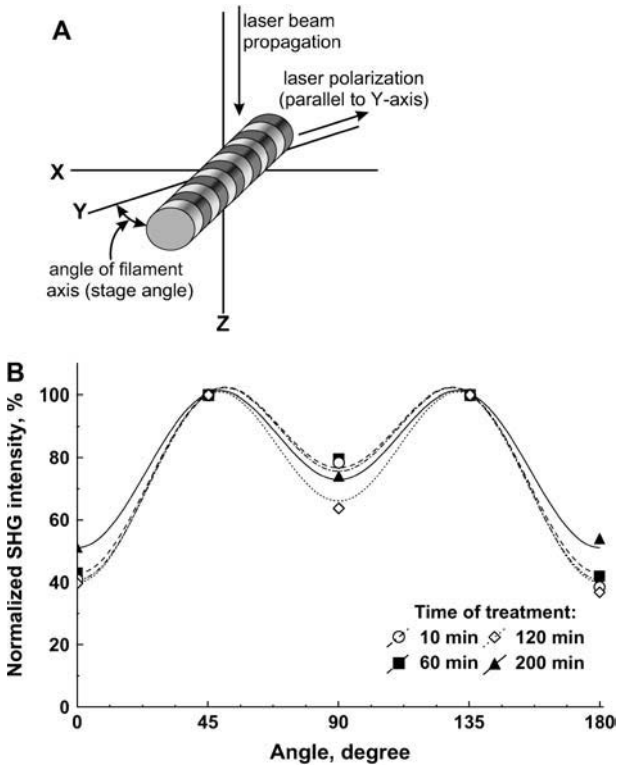

FIGURE 6 Polarization dependence of SHG intensity used to compare the molecular organization in sarcomeres before and after clearing. (*A*) The relevant axes of the laser propagation and laser polarization and the fiber axis. (*B*) The resulting SHG intensity as a function of the angle between the fibers and laser polarization. The data are plotted for the same time points as in Fig 1. No systematic variation is seen between the time points.

after glycerol treatment. These results essentially parallel those of Tromberg and co-workers obtained in the backward geometry (28), with the exception that no significant effect on the fibrillar pattern is observed in the forward-directed signal. We still conclude that collagen-based tissues are greatly disrupted by the application of glycerol and useful clearing is not observable by the SHG imaging modality. These results suggest that the optical clearing process in collagen is not simply due to refractive index matching but may involve a change in the supramolecular structure. Moreover, this change in assembly is not visible by either transmitted light or OCT measurements.

DISCUSSION

We have shown that treatment of muscle tissue with glycerol results in greatly increased SHG imaging depth and image quality. Here we consider the factors that are responsible for the achievable imaging depths in both the control and cleared tissue. First we addressed the attainable depth in the uncleared tissue. The reduced scattering coefficient, μ_s', in muscle at 900 nm is ~0.5 mm^{-1} (39), and for comparison with our experimental findings, Fig. 2 also shows the

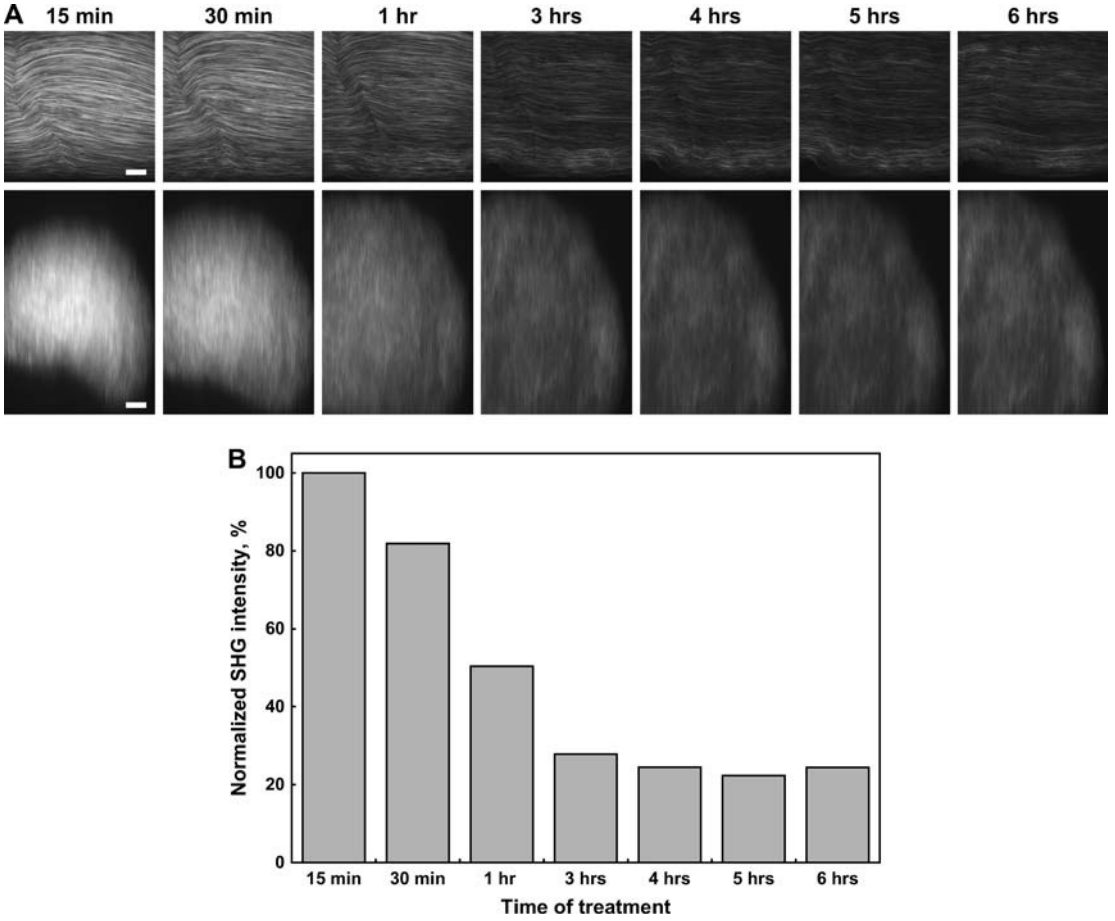

FIGURE 7 SHG imaging shows that 50% glycerol treatment of tendon has highly adverse effects and does not result in improved penetration. The top and bottom panels of Fig. 7 *a* show the time course of a single optical section and the *x-z* projections, respectively. A histogram of the SHG intensities over the time course is shown Fig. 7 *b* and a fivefold loss of intensity is observed.

expected depth-dependent decrease in intensity based solely on this value (*dashed line*). Yet we observe much more rapid attenuation with increasing depth in the control tissue, and we conclude that significant absorption of the SHG signal occurs. This is reasonable since the SHG wavelength is 450 nm and its absorption by cytochromes and heme proteins is expected to be significant. Indeed, a similar secondary inner filter effect was also recently observed by Rothstein et al. (40) in mouse skeletal muscle in vivo, where significant absorption of NADH autofluorescence was seen in this same wavelength range of our SHG signal. In the case here, the glycerol treatment permeabilizes the cell membranes, resulting in leakage of strongly absorbing cytoplasmic proteins out of the cell and thus lower intracellular optical density. The secondary inner filter effect on the SHG signal is then likely reduced, and increased imaging depth is observed.

To investigate if this is indeed the major mechanism responsible for the optical clearing in muscle, we treated muscle tissue with a mixture of 4% paraformaldehyde and 0.5% gluteraldehyde to cross-link the intracellular proteins and prevent or minimize protein leaching out of the cells. 3-D stacks of 50% glycerol-treated muscle were then acquired over a 24 h time course (as in Fig. 1), and the resulting *x-z* projection is shown in Fig. 8. Little clearing occurs relative to the data in Fig. 1 (without fixation), as only a slight increase (~10%) in SHG intensity is observed in the middle of the stack from fixed tissue. This measurement shows that the primary mechanism for clearing in muscle is indeed the loss of cytoplasmic protein, an effect that is abolished by fixation of protein in place.

Reports of optical clearing in collagen-based tissues have suggested refractive index matching plays a dominant role (24,26) where the matching can arise from the surface of the glass substrate and the tissue. In the case of muscle, where the glycerol breaks down the cell membranes (which also reduces the protein concentration), index matching could also occur by replacement of water with glycerol. However, we obtained the same imaging depths of ~200 microns for 25%, 50%, and 75% glycerol-treated muscle. The higher concentrations of glycerol must result in higher intracellular refractive indices, but the degree of clearing was the same. Although we have not found a published refractive index of

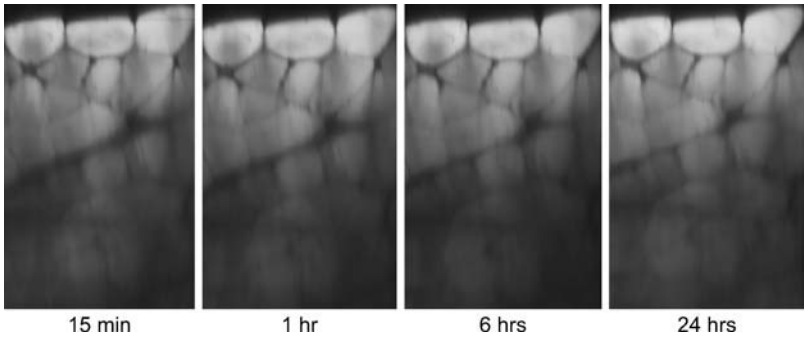

FIGURE 8 SHG imaging of mouse muscle tissue treated with 50% glycerol, 4% paraformaldehyde, and 0.5% gluteraldehyde, with the resulting x-z projections at 15 min, 1 h, 6 h, and 24 h. Little clearing is observed, indicating the mechanism arises from loss of cytoplasmic protein and decreased inner filter effect.

muscle at 900 nm, the refractive index of muscle at 632 nm has been reported to be ~1.38 (41) and is comparable to the 50% glycerol case. However, given the similarity of imaging depths with these three glycerol treatments, we can conclude that index matching only plays a small role in the optical clearing of muscle. This in conjunction with the lack of clearing upon fixation allows us to assign the reduction of the inner filter effect as the predominant mechanism for the increased imaging depth.

A complicating aspect in the interpretation of the SHG imaging depth profile lies in the competing effects of loss of input laser intensity and absorption of the output SHG signal, where the relative contributions change through the axial profile of the specimen. For example, as the laser propagates further into the tissue, the loss of laser intensity, and thus second harmonic production, decreases. Near the top of the specimen, the laser is less scattered; however, the desired SHG wave must propagate through the axial dimension to be detected and undergoes substantial absorption. By contrast, SHG produced near the bottom of the stack will undergo less absorption. Additionally, the loss of laser intensity will have a quadratic effect, whereas the absorption of the SHG is a linear process. Careful examination of the control and optically cleared data ($n = 12$ and 14 trials, respectively) in Fig. 2 reveals two distinct regimes, separating at ~40 microns. Near the top of the axial profile, the measured SHG intensity deviates greatly from the single exponential fit, where the decay is more rapid than predicted by the overall fit, showing the strong absorption contribution to the signal intensity in this region. Although the optically cleared data also deviate from the fit, they do so somewhat less dramatically, suggesting the role of a reduced inner filter effect. Both data sets are well fit to the single exponential near the bottom of the stack where scattering of the laser will be the predominant loss mechanism. Furthermore, although SHG produced from these regions will experience less absorption upon propagation through the specimen, the reduction in the inner filter further reduces these losses.

Although differing in mechanism, it is illustrative to compare the SHG optical clearing in muscle in this work with reports on other modalities in collagen-based tissues. Comparable values of 2–3 in increased penetration depth via glycerol treatment were also found by Welch and co-workers in their investigation of rat skin with OCT (24). Similarly, Khan et al. recently defined an optical clearing potential (OCP) as the ratio of reduced scattering coefficients in cleared and uncleared samples and using linear transmission measurements found values in the range 100–300% for skin treated with a variety of hyperosmotic reagents, including glycerol, dialcohols, and organic acids (23). Although these values are comparable, the mechanisms differ substantially. Both this work and that of Tromberg have shown through SHG imaging that the optical clearing process with glycerol has strong adverse effects on collagen-based tissues, whereas transmitted light and OCT are not sensitive to the underlying structural changes.

Ultimately, optical clearing may become useful in clinical diagnostics to increase imaging depth and image quality. Muscle biopsies can be examined with forward-directed SHG, and the increase of several hundred microns attainable in imaging depth can significantly improve the image information content from a single specimen. Alternatively, backscattered SHG could be used for imaging skin pathologies in vivo. Although most optical clearing studies to date have used OCT, and this modality is already used in certain clinical applications (retinal and esophageal imaging), SHG may be a better tool for many applications. This is true because SHG is intrinsically more sensitive to molecular and supramolecular organization than OCT and additionally has superior axial resolution.

Because of the adverse effects of glycerol treatment on SHG imaging of collagen-based tissues, clearing of such tissues with other hyperosmotic agents should be investigated. For example, sugar alcohols have been used for optical clearing studies in transmitted light imaging and perhaps agents of these types and/or others could be applied to collagen-based structures and achieve clearing while not adversely affecting the quarternary structure. For example, Tuchin and co-workers measured and modeled the diffusion of mannitol and glucose through human dura mater and observed significant clearing where they considered the clearing effect to arise from refractive index matching (26). Khan et al. examined the OCP of several reagents, including dialcohols with transmitted light imaging (23), but the effects

of these reagents have not yet been probed by SHG imaging to examine the effects on the supramolecular organization.

CONCLUSIONS

Using glycerol as an optical clearing agent, we can achieve a 2.5-fold increase in achievable SHG imaging depth in skeletal muscle, This improvement occurs with little change in the SHG intensity or sarcomere morphological structure to indicate damage to the tertiary or quarternary structure of the acto-myosin complexes. The similarity of the polarization profile of the control and cleared muscle tissue further supports this finding. We suggest that the primary mechanism of glycerol-based optical clearing in muscle results from the reduction of cytoplasmic protein concentration and concomitant decrease in secondary inner filter effect on the SHG signal. The lack of dependence on glycerol concentration for the imaging depth indicates that refractive index matching plays only a minor role in the optical clearing of muscle. Although the initial use of glycerol extraction of muscle fibers in the 1950s was not for imaging applications, our quantitative analyses of 3-D SHG imaging data reaffirm the conclusion that the contractile structure is essentially unchanged. The use of appropriate agents may become a general method for increasing transparency in thick tissues imaged by these modalities. However, we find experimentally that the benefits of optical clearing for SHG are much greater in muscle than in collagen-based tissues.

P.J.C. and W.A.M. gratefully acknowledge support under National Institutes of Health EB-1842. W.A.M. is also supported by a New Scholar in Aging award from the Ellison Medical Foundation. S.P. acknowledges support from the American Heart Association.

REFERENCES

1. Campagnola, P. J., A. C. Millard, M. Terasaki, P. E. Hoppe, C. J. Malone, and W. A. Mohler. 2002. Three-dimensional high-resolution second-harmonic generation imaging of endogenous structural proteins in biological tissues. *Biophys. J.* 82:493–508.
2. Campagnola, P. J., and L. M. Loew. 2003. Second-harmonic imaging microscopy for visualizing biomolecular arrays in cells, tissues and organisms. *Nat. Biotechnol.* 21:1356–1360.
3. Chu, S. W., I. H. Chen, T. M. Liu, C. K. Sun, S. P. Lee, B. L. Lin, P. C. Cheng, M. X. Kuo, D. J. Lin, and H. L. Liu. 2002. Nonlinear biophotonic crystal effects revealed with multimodal nonlinear microscopy. *J. Microsc.* 208:190–200.
4. Moreaux, L., O. Sandre, and J. Mertz. 2000. Membrane imaging by second-harmonic generation microscopy. *J. Opt. Soc. Am. B.* 17:1685–1694.
5. Zoumi, A., A. Yeh, and B. J. Tromberg. 2002. Imaging cells and extracellular matrix in vivo by using second-harmonic generation and two-photon excited fluorescence. *Proc. Natl. Acad. Sci. USA.* 99: 11014–11019.
6. Cox, G., E. Kable, A. Jones, I. Fraser, F. Manconi, and M. D. Gorrell. 2003. 3-Dimensional imaging of collagen using second harmonic generation. *J. Struct. Biol.* 141:53–62.
7. Williams, R. M., W. R. Zipfel, and W. W. Webb. 2005. Interpreting second harmonic generation images of collagen I fibrils. *Biophys. J.* 88:1377–1386.
8. Muller, M., J. A. Squier, T. Wilson, and G. Brakenhoff. 1998. 3D microscopy of transparent objects using third-harmonic generation. *J. Microsc.* 191:266–272.
9. Sun, C.-K., S.-W. Chu, S.-Y. Chen, T.-H. Tsai, T.-M. Liu, C.-Y. Lin, and H.-J. Tsai. 2004. Higher harmonic generation microscopy for developmental biology. *J. Struct. Biol.* 147:19–30.
10. Cheng, J.-X., A. Volkmer, L. D. Book, and X. S. Xie. 2001. An epi-detected coherent anti-Stokes Raman scattering (E-CARS) microscope with high spectral resolution and high sensitivity. *J. Phys. Chem. B.* 105:1277–1280.
11. Cheng, J. X., Y. K. Jia, G. Zheng, and X. S. Xie. 2002. Laser-scanning coherent anti-Stokes Raman scattering microscopy and applications to cell biology. *Biophys. J.* 83:502–509.
12. Wurpel, G. W. H., J. M. Schins, and M. Mueller. 2002. Chemical specificity in three-dimensional imaging with multiplex coherent anti-Stokes Raman scattering microscopy. *Opt. Lett.* 27:1093–1095.
13. Campagnola, P. J., M. D. Wei, A. Lewis, and L. M. Loew. 1999. High resolution non-linear optical microscopy of living cells by second harmonic generation. *Biophys. J.* 77:3341–3349.
14. Reference deleted in proof.
15. Stoller, P., B.-M. Kim, A. M. Rubinchik, K. M. Reiser, and L. B. Da Silva. 2001. Polarization-dependent optical second-harmonic imaging of a rat-tail tendon. *J. Biomed. Opt.* 7:205–214.
16. Yeh, A. T., N. Nassif, A. Zoumi, and B. J. Tromberg. 2002. Selective corneal imaging using combined second-harmonic generation and two-photon excited fluorescence. *Opt. Lett.* 27:2082–2084.
17. Chu, S.-W., S.-Y. Chen, G.-W. Chern, T.-H. Tsai, Y.-C. Chen, B.-L. Lin, and C.-K. Sun. 2004. Studies of $\chi^{(2)}/\chi^{(3)}$ tensors in submicron-scaled bio-tissues by polarization harmonics optical microscopy. *Biophys. J.* 86:3914–3922.
18. Mohler, W., A. C. Millard, and P. J. Campagnola. 2003. Second harmonic generation imaging of endogenous structural proteins. *Methods.* 29:97–109.
19. Zipfel, W. R., R. M. Williams, R. Christie, A. Y. Nikitin, B. T. Hyman, and W. W. Webb. 2003. Live tissue intrinsic emission microscopy using multiphoton-excited native fluorescence and second harmonic generation. *Proc. Natl. Acad. Sci. USA.* 100:7075–7080.
20. Brown, E., T. McKee, E. diTomaso, A. Pluen, B. Seed, Y. Boucher, and R. K. Jain. 2003. Dynamic imaging of collagen and its modulation in tumors in vivo using second-harmonic generation. *Nat. Med.* 9: 796–800.
21. Zoumi, A., X. Lu, G. S. Kassab, and B. J. Tromberg. 2004. Imaging coronary artery microstructure using second-harmonic and two-photon fluorescence microscopy. *Biophys. J.* 87:2778–2786.
22. Khan, M. H., B. Choi, S. Chess, K. M. Kelly, J. McCullough, and J. S. Nelson. 2004. Optical clearing of in vivo human skin: implications for light-based diagnostic imaging and therapeutics. *Lasers Surg. Med.* 34:83–85.
23. Khan, M. H., S. Chess, B. Choi, K. M. Kelly, and J. S. Nelson. 2004. Can topically applied optical clearing agents increase the epidermal damage threshold and enhance therapeutic efficacy? *Lasers Surg. Med.* 35:93–95.
24. Vargas, G., E. K. Chan, J. K. Barton, H. G. Rylander 3rd, and A. J. Welch. 1999. Use of an agent to reduce scattering in skin. *Lasers Surg. Med.* 24:133–141.
25. Tuchin, V. V., X. Q. Xu, and R. K. Wang. 2002. Dynamic optical coherence tomography in studies of optical clearing, sedimentation, and aggregation of immersed blood. *Appl. Opt.* 41:258–271.
26. Bashkatov, A. N., E. A. Genina, Y. P. Sinichkin, V. I. Kochubey, N. A. Lakodina, and V. V. Tuchin. 2003. Glucose and mannitol diffusion in human dura mater. *Biophys. J.* 85:3310–3318.
27. Xu, X. Q., R. K. Wang, and J. B. Elder. 2003. Optical clearing effect on gastric tissues immersed with biocompatible chemical agents investigated by near infrared reflectance spectroscopy. *J. Phys. D: Appl. Phys.* 36:1707–1713.

28. Yeh, A. T., B. Choi, J. S. Nelson, and B. J. Tromberg. 2003. Reversible dissociation of collagen in tissues. *J. Invest. Dermatol.* 121:1332–1335.

29. Szent-Gyorgyi, A. 1949. Free-energy relations and contraction of actomyosin. *Biol. Bull.* 96:140–161.

30. Finck, H., H. Holtzer, and J. J. Marshall. 1956. An immunochemical study of the distribution of myosin in glycerol extracted muscle. *J. Biophys. Biochem. Cytol.* 2:175–178.

31. Huxley, H. E. 1957. The double array of filaments in cross-striated muscle. *J. Biophys. Biochem. Cytol.* 3:631–648.

32. Nayler, W. G., and N. C. Merrillees. 1964. Some observations on the fine structure and metabolic activity of normal and glycerinated ventricular muscle of toad. *J. Cell Biol.* 22:533–550.

33. Sarkar, N., A. Szent-Gyorgyi, and L. Varga. 1950. Adenosintriphosphatase activity of the glycerol extracted muscle fibres. *Enzymologia.* 14:267–271.

34. Lorand, L., and C. Moos. 1957. Studies on the biochemistry of contraction and relaxation in glycerinated muscle; the effects of phosphoenolpyruvate. *Biochim. Biophys. Acta.* 24:461–474.

35. Lemire, D., C. Pharand, J. C. Rajaonah, B. Dube, and A. R. LeBlanc. 2000. Wavelet time entropy, T wave morphology and myocardial ischemia. *IEEE Trans. Biomed. Eng.* 47:967–970.

36. Tromberg, B. J., N. Shah, R. Lanning, A. Cerussi, J. Espinoza, T. Pham, L. Svaasand, and J. Butler. 2000. Non-invasive in vivo characterization of breast tumors using photon migration spectroscopy. *Neoplasia.* 2:26–40.

37. Dunn, A. K., V. P. Wallace, M. Coleno, M. W. Berns, and B. J. Tromberg. 2000. Influence of optical properties on two-photon fluorescence imaging in turbid samples. *Appl. Opt.* 39:1194–1201.

38. Plotnikov, S., A. C. Millard, P. J. Campagnola, and W. A. Mohler. 2005. Characterization of the myosin-based source for second-harmonic generation from muscle sarcomeres. *Biophys. J.* In press.

39. Kienle, A., L. Lilge, M. S. Patterson, R. Hibst, R. Steiner, and B. C. Wilson. 1996. Spatially resolved absolute diffuse reflectance measurements for noninvasive determination of the optical scattering and absorption coefficients of biological tissue. *Appl. Opt.* 35:2305–2314.

40. Rothstein, E. C., S. Carroll, C. A. Combs, P. D. Jobsis, and R. S. Balaban. 2005. Skeletal muscle NAD(P)H two-photon fluorescence microscopy in vivo: topology and optical inner filters. *Biophys. J.* 88:2165–2176.

41. Tearney, G. J., M. E. Brezinski, J. F. Southern, B. E. Bouma, M. R. Hee, and J. G. Fujimoto. 1995. Determination of the refractive index of highly scattering human tissue by optical coherence tomography. *Opt. Lett.* 20:2258–2260.